Journal of Sustainability for Energy
https://www.acadlore.com/journals/JSE

Charging Rate and Storage Capacity Tradeoffs in Composite Cold Thermal Energy Storage for Sustainable Cooling

R. Ghasemi*

Faculty of Mechanical Engineering, Technische Universität Braunschweig, 38106 Braunschweig, Germany

* Correspondence: R. Ghasemi (R.ghasemi@tu-braunschweig.de)

Received: 08-20-2026 **Revised:** 11-02-2026 **Accepted:** 11-09-2026

Citation: R. Ghasemi, "Charging rate and storage capacity tradeoffs in composite cold thermal energy storage for sustainable cooling," *J. Sustain. Energy*, vol. 5, no. 4, pp. 338–351, 2026. https://doi.org/10.56578/jse050405.

© 2026 by the author(s). Published by Acadlore Publishing Services Limited, Hong Kong. This article is available for free download and can be reused and cited, provided that the original published version is credited, under the CC BY 4.0 license.

Abstract: Cold thermal energy storage supports sustainable cooling by separating cold production from demand, while conductive additives alter both charging performance and material requirements. This study investigates how ternary particles and a copper network affect freezing time, retained latent capacity, and composite mass in a wavy-walled water-based storage cell with two cooled fins. A conservative finite-volume enthalpy model was used to evaluate 12 combinations of TiO_2–Ag–Al_2O_3 particle loading and porosity. Numerical verification included comparison with a two-phase Stefan solution and refinement of the spatial grid, time step, and phase-change temperature interval. Skeleton-conductance sensitivity was also assessed. Under the nominal conditions, the times to reach a mean solid fraction of 0.99 were 64.92 s for water, 55.95 s for particles alone, 15.14 s for foam alone, and 14.12 s for the combined medium. The combined configuration shortened freezing by 78.25%, retained 90.73% of the water-baseline volumetric latent capacity, and achieved an average latent charging index 4.17 times the baseline value. Adding particles to the foam shortened freezing by a further 6.76%; however, the foam-only medium stored more latent cooling after 10 s, at 273.92 versus 268.29 MJ·m^{-3}. At equal full latent capacity, the combined medium required 10.22% more material volume and 78.78% more composite mass than water. These findings identify charging deadlines and required storage capacity as joint criteria for conductive-material allocation. The analysis provides a quantitative basis for balancing charging performance and material requirements in cold thermal energy storage for sustainable cooling.

Keywords: Cold thermal energy storage; Sustainable cooling; Phase change materials; Metal foam; Charging rate; Material allocation

1 Introduction

Cold thermal energy storage separates cooling production from cooling demand. Its value depends on both the amount of cooling retained and the time needed to establish that inventory. A store that freezes within a short production window can be scheduled differently from one that requires prolonged refrigeration. Reviews of cold-storage control and materials therefore connect transient thermal performance with equipment operation and the timing of electricity use [1–3]. For sustainable cooling, this connection makes charging duration and resource allocation complementary design variables.

Water offers a large latent heat near a temperature useful for ice storage. During charging, heat must travel from the remaining liquid through a growing solid region to the cooled surfaces. A substantial latent capacity can consequently coexist with a long freezing period. Experiments and numerical studies of building cooling stores, together with discharge assessments, distinguish the stored inventory from its rate of access [4, 5]. The material and geometry selected for a store should therefore be evaluated against the available charging period as well as its eventual cooling duty.

Thermal transport can be modified through dispersed particles, extended surfaces, and conductive porous structures [6–8]. These measures act differently. Nanoparticles change the effective properties of the phase-changing medium, whereas fins and metal foam extend conductive paths into the enclosure. A recent review of foam–phase change composites emphasizes the dependence on structural parameters and the thermal model used to represent them [9]. Effective-conductivity studies connect that dependence to network topology and to the correlation used

for the composite medium [10, 11]. Conductive additions also occupy space and contribute mass, so their charging response must be considered alongside the retained phase-changing material.

Fin–foam cold-storage studies examine how conductive paths intersect regions of residual liquid [12]. Related work addresses melting in fin–foam structures, solidification with branch-shaped fins and nanoparticles, and composite media in triplex-tube heat exchangers [13–15]. Investigations covering complete melting–solidification cycles and experimentally assessed fin–foam arrangements show why performance must be interpreted within the chosen geometry and thermal boundary conditions [16, 17]. Ice-storage experiments with copper foam and studies of partial filling further identify the distribution of metal as a design variable [18, 19]. Cycle-level investigations extend this question to the charging and discharging sequence [20].

Particle-containing media introduce a second material allocation. Experiments with graphene-based water suspensions and functionalized graphene–CuO mixtures assess stability and phase-change behavior alongside thermal transport [21, 22]. Studies of other nanocomposite storage materials and TiO_2–Ag dispersions similarly connect composition with thermal properties and stability [23, 24]. Thermophysical compilations for ternary mixtures provide constituent-property inputs for multicomponent media [25]. For storage design, the volume occupied by particles also changes the amount of water available to freeze, while the density of the particles changes capacity per unit composite mass.

Combined particle and foam arrangements already have relevant precedents. Mirparizi investigated ternary particles and metal foam in cold storage [26], and Shafee considered a wavy-walled enclosure with internal fins and a porous ternary medium [27]. Studies of radiative finned storage, nanoparticle-assisted freezing, and tree-finned composite enclosures provide further comparisons [28–30]. These precedents establish the thermal mechanism of combined conductive measures. The remaining design question addressed here is how the separate and joint material additions compare when freezing time, latent inventory, composite mass, and a finite charging deadline are evaluated on the same basis.

The present study defines a two-dimensional conduction benchmark with a wavy wall, two cooled internal fins, water, equal-volume TiO_2–Ag–Al_2O_3 particles, and a copper skeleton. A four-by-three matrix of total particle fraction and porosity separates particle addition from foam incorporation. A foam-only control completes the comparison between the four endpoint material states. A conservative enthalpy calculation is checked against a two-phase Stefan solution and examined through mesh, time-step, and phase-interval refinement. The resulting fields and response measures are then used to evaluate material allocation for scheduled cooling production. The analysis resolves three related design choices: the incremental value of particles after a copper network is installed, the composition that establishes the largest latent inventory by a fixed deadline, and the volume and mass required to retain a specified latent capacity. Skeleton-conductance sensitivity establishes how these comparisons depend on the effective-network representation.

2 Model and Computational Procedure

2.1 Reference Cell and Thermal Conditions

Figure 1 defines the reference storage cell. Its height H is 6.00 mm, mean width W is 3.00 mm, and right-wall amplitude a is 0.30 mm. Three complete waves occur over the height. The outer wall is specified by Eq. (1). Two straight fins extend 1.50 mm from the left boundary. Each fin is 0.375 mm thick, and its centerline lies at $y = H/4$ or $3H/4$. The storage region is the space between the outer boundary and the fin surfaces. All capacities below refer to this region; the fins are part of the imposed thermal boundary.

$$x_w(y) = W + a\cos(6\pi y/H), \quad 0 \le y \le H \tag{1}$$

The cell starts uniformly at 274.15 K. The left wall and both fin surfaces are held at 268.15 K from the start of charging. The wavy wall and the top and bottom boundaries are adiabatic. The water phase-change temperature is 273.15 K. These conditions define an idealized conduction-controlled charging duty, with one kelvin of initial liquid superheat. The millimetre-scale cell provides a reference geometry for comparing materials under identical thermal forcing. Table 1 lists the geometrical and operating inputs.

Thermal transport is represented by a stationary medium with a scalar effective conductivity. The particles are uniformly distributed, and the pore medium and copper skeleton share a local temperature. Water mass is tracked on a fixed reference-volume basis using ρ_0 = 1000 kg·m^{-3} in both thermal states. Separate solid and liquid heat capacities and conductivities describe sensible transport. The common-temperature assumption gives a local-thermal-equilibrium representation of the pore medium and copper network.

2.2 Material Fractions and Effective Properties

The total particle volume fraction ϕ is defined within the pore medium. TiO_2, Ag, and Al_2O_3 each occupy a final volume fraction $v_i = \phi/3$, so the water fraction in the pore medium is $1-\phi$. Porosity γ is the pore-medium fraction

of the storage-region volume. The water, particle, and copper fractions per unit storage-region volume are therefore $\gamma(1-\phi)$, γv_i, and $1-\gamma$, respectively. Their sum is unity. The parameter matrix uses ϕ = 0, 0.015, 0.030, and 0.045 with γ = 1, 0.975, and 0.95.

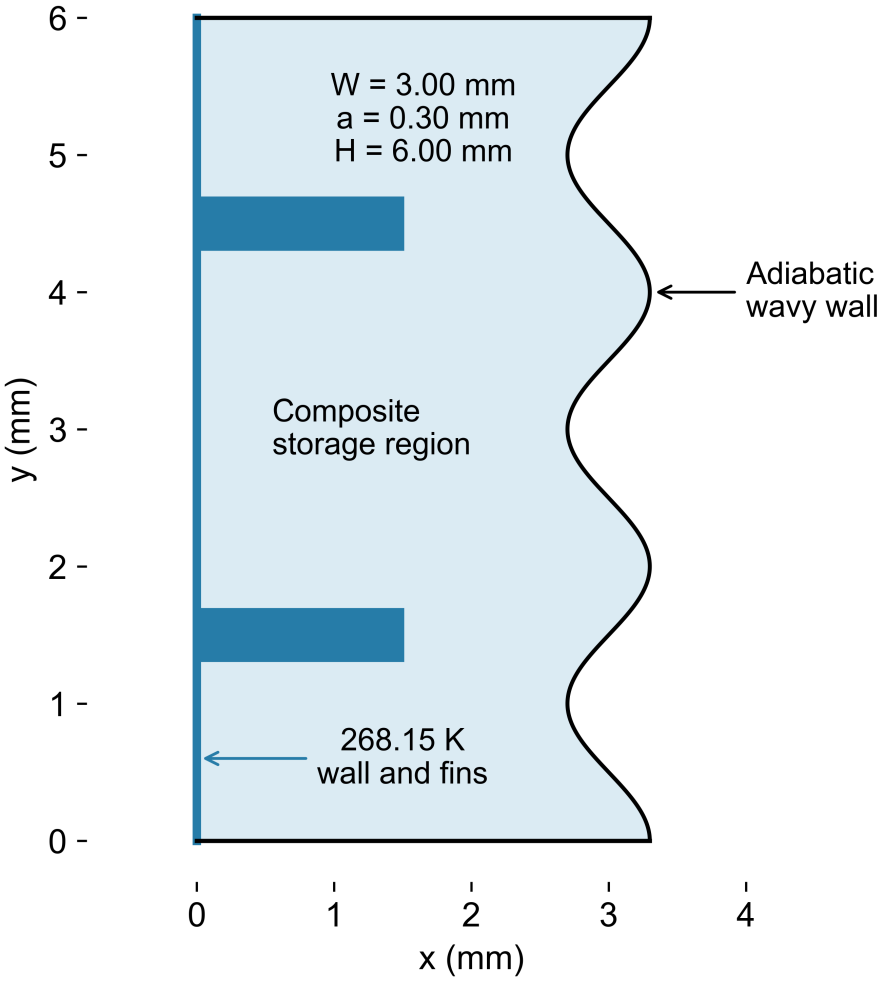


Figure 1. Reference-cell geometry and thermal boundary conditions
Note: W = mean width; a = wave amplitude; H = height.

Table 1. Reference-cell geometry and charging conditions

Input	Value
Height H	6.00 mm
Mean width W; wave amplitude a	3.00 mm; 0.30 mm
Waves along height	3
Fin length; thickness	1.50 mm; 0.375 mm
Fin centerlines	$H/4$ and $3H/4$
Initial temperature; phase-change temperature	274.15 K; 273.15 K
Cooled wall and fin temperature	268.15 K
Other outer boundaries	Adiabatic
Particle fractions ϕ; porosities γ	0, 0.015, 0.030, 0.045; 1, 0.975, 0.95
Nominal skeleton factor η; phase interval δ	1/3; 0.10 K

Table 2 gives the constant reference properties used in the calculation. Water and ice property values are selected as rounded near-freezing benchmark inputs, informed by phase-change modeling and reference-property literature [31–33]. Particle properties follow the ternary-material compilation in Al-Kouz et al.'s work [25]. Copper is assigned 8,960 kg·m^{-3}, 385 J·kg^{-1}·K^{-1}, and 400 W·m^{-1}·K^{-1} as fixed benchmark inputs. The volumetric heat capacities C_s and C_l, volumetric latent heat Λ, and composite reference density ρ_β are calculated from Eqs. (2) and (3). The

subscript j distinguishes the solid and liquid thermal states, and the index i denotes the three particle species.

Table 2. Constituent thermophysical properties used in the numerical model

Constituent	ρ ($\mathrm{kg \cdot m^{-3}}$)	c ($\mathrm{J \cdot kg^{-1} \cdot K^{-1}}$)	k ($\mathrm{W \cdot m^{-1} \cdot K^{-1}}$)
Water, liquid	1,000	4,217	0.57
Water, solid reference	1,000	2,100	2.2
TiO_2	4,250	690	8.953
Ag	10,500	235	429
Al_2O_3	3,970	765	40
Copper	8,960	385	400

Note: The latent heat of water is 333.6 kJ·kg^{-1}. A reference water density of 1,000 kg·m^{-3} is used in both thermal states.

$$C_j = \gamma \left[(1-\phi)\rho_0 c_j + \sum_{i=1}^{3} v_i \rho_i c_i \right] + (1-\gamma)\rho_{\mathrm{Cu}} c_{\mathrm{Cu}}, \quad j = s, l, \tag{2}$$

$$\Lambda = \gamma(1-\phi)\rho_0 L, \quad \rho_b = \gamma \left[(1-\phi)\rho_0 + \sum_{i=1}^{3} v_i \rho_i \right] + (1-\gamma)\rho_{\mathrm{Cu}} \tag{3}$$

The particle-containing medium is represented by the multi-inclusion Maxwell relation in Eq. (4). The three particle contributions enter through their final volume fractions in a common water matrix. The dilute spherical-inclusion approximation defines the conductive material comparison. Contact and interfacial resistance are important additional microstructural variables in dispersed composites [34]. The benchmark relation uses perfect particle–matrix thermal contact.

$$\beta_j = \sum_{i=1}^{3} v_i \frac{k_i - k_{w,j}}{k_i + 2k_{w,j}}, \quad k_{n,j} = k_{w,j} \frac{1+2\beta_j}{1-\beta_j}, \quad k_j = \gamma k_{n,j} + \eta(1-\gamma)k_{\mathrm{Cu}} \tag{4}$$

The copper contribution contains a skeleton conductivity factor η. For an ideal network with equal copper allocation along three orthogonal directions, one third of the copper conducts along each coordinate direction, giving the nominal value η = 1/3 in Eq. (4). This geometric allocation defines the reference network. Topology-dependent conductivity correlations and comparisons with composite-material experiments establish the importance of the network representation [10, 11]. Sensitivity calculations use η = 0.10, 1/3, and 1.00; the last value is the directional parallel-path reference. Porosity sets the copper and pore-medium volumes, while η sets the conductance associated with the copper allocation.

The effective conductivities are also compared with the series and parallel limits for the same two constituent phases. The series limit is $[\gamma/k_{n,j} + (1-\gamma)/k_{\mathrm{Cu}}]^{-1}$, and the parallel limit is $\gamma k_{n,j} + (1-\gamma)k_{\mathrm{Cu}}$. Here $k_{n,j}$ is the pore-medium conductivity in thermal state j. At γ = 0.95, the foam-only liquid conductivity is 7.20 $\mathrm{W \cdot m^{-1} \cdot K^{-1}}$, between limits of 0.600 and 20.542 $\mathrm{W \cdot m^{-1} \cdot K^{-1}}$; the corresponding solid conductivity is 8.757 $\mathrm{W \cdot m^{-1} \cdot K^{-1}}$, between 2.315 and 22.090 $\mathrm{W \cdot m^{-1} \cdot K^{-1}}$. For the combined medium, the liquid and solid conductivities are 7.279 and 8.985 $\mathrm{W \cdot m^{-1} \cdot K^{-1}}$. All 24 nominal conductivities across the 12 material combinations and two thermal states lie within their respective series and parallel limits.

2.3 Conservative Enthalpy Formulation

A continuous phase relation links temperature and local solid fraction through Eq. (5). The transition interval has full width δ, with $T_s = T_m - \delta/2$ and $T_l = T_m + \delta/2$. The nominal two-dimensional calculations use δ = 0.10 K. Solid fraction equals unity below T_s and zero above T_l. Its intermediate values describe the regularized phase transition.

$$\begin{aligned} S(T) &= 1, \quad \text{for } T < T_S \\ S(T) &= (T_l - T)/\delta, \quad \text{for } T_S \le T \le T_l \\ S(T) &= 0, \quad \text{for } T > T_l \end{aligned} \tag{5}$$

The volumetric enthalpy in Eq. (6) uses the fully solid state at T_s as its reference. The interval slope is $M = (C_s + C_l)/2 + \Lambda/\delta$. Both enthalpy and temperature remain continuous across the two interval boundaries.

The resulting balance, Eq. (7), includes the latent inventory and the sensible heat of all constituents. This conservative form is consistent with the emphasis on enthalpy conservation in recent phase-change methods [35–37] and composite-storage calculations [38, 39].

$$\begin{aligned} \mathcal{H}(T) &= C_s\,(T - T_s)\,, \quad \text{for } T < T_s, \\ \mathcal{H}(T) &= M\,(T - T_s)\,, \quad \text{for } T_s \le T \le T_l, \\ \mathcal{H}(T) &= M\delta + C_l\,(T - T_l)\,, \quad \text{for } T > T_l. \end{aligned} \tag{6}$$

$$\frac{\partial \mathcal{H}}{\partial t} = \nabla \cdot (k \nabla T), \quad k = S k_s + (1 - S) k_l \tag{7}$$

The conductivity interpolates between the effective solid and liquid values through the local solid fraction. The same temperature determines enthalpy, phase fraction, and conductivity. This common state relation provides a direct connection between the plotted temperature and solid-fraction fields.

2.4 Spatial Discretization and Nonlinear Solution

The equations are discretized by a cell-centered finite-volume method on a uniform Cartesian grid. The wavy wall and the fin slots are represented by the active-cell mask. Internal face conductivities use harmonic averaging. The prescribed-temperature wall and fin faces use the half-cell distance to the boundary; adiabatic faces contribute zero heat flux. Every internal face contributes equal and opposite heat exchange to its neighboring cells. Equation (8) gives the control-volume update, where G_f is the face conductance and V_i is the cell volume per unit out-of-plane depth.

$$\mathcal{H}_i^{n+1} - \mathcal{H}_i^n = \frac{\Delta t}{V_i} \sum_{f \in \partial V_i} G_f^n \left(T_{nb(f)}^{n+1} - T_i^{n+1} \right) \tag{8}$$

The enthalpy difference is evaluated at the new temperature, and face conductivities are evaluated from the preceding time level. This semi-implicit treatment gives a nonlinear enthalpy solve at each step while retaining the same face fluxes in the heat balance. A damped Newton iteration uses the exact piecewise derivative of enthalpy. Sparse linear systems are solved directly, and a residual-based line search selects the Newton step. The maximum local residual divided by Λ must be below 10^{-10}. The implementation permits up to 60 iterations and halves the step following an unsuccessful solve.

The nominal grid has 96 cells along the height, giving Δx = Δy = 62.5 μm. The nominal time step is 0.05 s. Mesh tests use 64, 96, 128, and 192 cells along the height. Time-step tests use 0.10, 0.05, 0.025, and 0.0125 s; phase-interval tests use 0.20, 0.10, and 0.05 K. The two endpoint materials are examined separately. Fin thickness and position coincide with grid faces for all four tested meshes. The changing Cartesian representation of the curved wall is included in the mesh comparison.

Cumulative heat extraction is calculated from the same boundary-face fluxes used in the update. It is compared with the volume integral of the enthalpy decrease at every recorded time. The reported energy residual is their absolute difference divided by the enthalpy decrease. This is a discrete conservation check, complementary to the independent analytical comparison in Section 3.1. The supplementary material contains the solver, all input settings, numerical outputs, and figure scripts.

2.5 Charging and Material-Allocation Measures

The mean solid fraction and the 99% freezing time are defined in Eq. (9). Linear interpolation between the two time samples bracketing a mean solid fraction of 0.99 determines t_{99}. This common endpoint gives all material cases the same completion criterion. Phase-fraction measurements in the wider phase change material literature likewise illustrate the value of phase fraction as an observable distinct from temperature [40].

$$\bar{S}(t) = \frac{1}{V} \int_V S(\mathbf{x}, t) dV, \quad t_{99} = \inf\{t : \bar{S}(t) \ge 0.99\} \tag{9}$$

Eq. (10) defines the full latent capacity per unit storage-region volume, the latent cooling established by time t, the average latent charging index up to t_{99}, and latent capacity per unit composite mass. The factor 0.99 in P_{99} makes the index correspond to the selected endpoint. Sensible cooling is included in the governing enthalpy balance, while these measures isolate the latent component used for material comparison.

$$q_{\text{lat}} = \Lambda, \quad q_{\text{stored}}\,(t) = \Lambda \bar{S}(t), \quad P_{99} = \frac{0.99\Lambda}{t_{99}}, \quad \ell = \frac{\Lambda}{\rho_b} \tag{10}$$

A time reduction is calculated as $100(1-t_{99,\text{case}}/t_{99,\text{reference}})$. Water is the reference for the overall material change. The nanoparticle-only medium is the reference for adding foam at unchanged pore composition, and the foam-only medium is the reference for adding particles at unchanged porosity. A finite charging window τ is evaluated through $q_{\text{stored}}(\tau)$. This separates an early charging advantage from the latent inventory available after a sufficiently long charging period.

3 Numerical Verification

3.1 Two-Phase Stefan Comparison

A one-dimensional freezing problem provides an independent check on the enthalpy implementation. The rod is 10 mm long, starts at 274.15 K, and has a left boundary at 268.15 K. The far boundary is insulated. Pure-water properties from Table 2 are used, with a 0.05 K phase interval. The analytical semi-infinite two-phase solution gives the interface position in Eq. (11). The positive parameter λ satisfies the Stefan heat balance in Eq. (12), where erf and erfcx are the error function and the scaled complementary error function. The interface remains well separated from the far boundary over the 20 s comparison period.

$$s(t) = 2\lambda\sqrt{\alpha_s t}, \quad \alpha_s = k_{w,s}/\left(\rho_0 c_s\right), \quad \alpha_l = k_{w,l}/\left(\rho_0 c_l\right) \tag{11}$$

$$\frac{k_{w,s}\left(T_m - T_c\right)e^{-\lambda^2}}{\sqrt{\pi\alpha_s}\,\operatorname{erf}(\lambda)} - \frac{k_{w,l}\left(T_i - T_m\right)}{\sqrt{\pi\alpha_l}\,\operatorname{erfcx}\left(\lambda\sqrt{\alpha_s/\alpha_l}\right)} = \rho_0 L\lambda\sqrt{\alpha_s} \tag{12}$$

Calculations used 300, 600, and 1200 cells with a 0.01 s time step. The numerical front was obtained by interpolating the $T = T_m$ crossing. For the 1200-cell calculation, the largest sampled front-position error over 1–20 s was 2.41%, and the error at 20 s was 0.22%. Table 3 reports every sampled time for this mesh. Figure 2 compares the three numerical resolutions with the analytical front and shows the temperature profile at 20 s. The analytical test checks the moving phase boundary and the temperature field, while the energy residual checks the discrete heat balance.

Table 3. Numerical and analytical phase-front positions for the two-phase Stefan problem using 1200 cells

Time (s)	Analytical Front (mm)	Numerical Front (mm)	Absolute Relative Error (%)
1	0.25182	0.24576	2.409
2	0.35613	0.35234	1.064
5	0.56309	0.55866	0.787
10	0.79633	0.79249	0.482
20	1.12619	1.12370	0.221

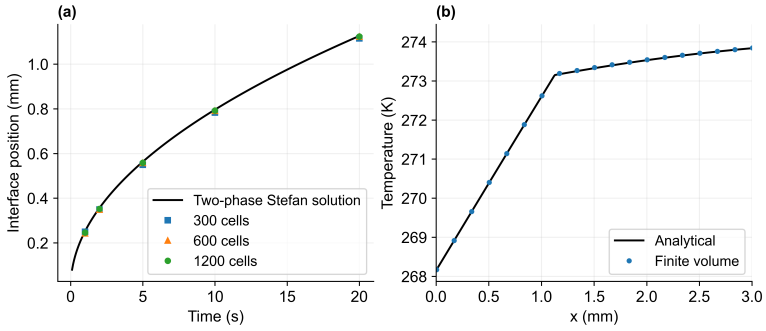


Figure 2. Two-phase Stefan verification: (a) phase-front position and (b) temperature profile at 20 s

3.2 Resolution and Conservation Checks

Table 4 lists the mesh comparison at a fixed 0.025 s time step. Relative to the 192-cell-height grid, the 96-cell-height grid changed t_{99} by 1.85% for water and 0.85% for the combined medium. The nominal 0.05 s time step changed t_{99} by 0.15% and 0.11% relative to 0.0125 s. Relative to a 0.05 K phase interval, the nominal 0.10 K interval

changed the corresponding times by -0.35% and -0.41%. Figure 3 summarizes the effects of grid resolution, time step, and phase-interval width on the 99% freezing time. The difference between the water and combined-medium freezing times remained substantially larger than the changes associated with numerical refinement.

Table 4. Mesh sensitivity of the 99% freezing time

Material	Height Cells	Active Cells	t_{99} (s)	Difference (%)
Water	64	1,920	65.9342	3.552
Water	96	4,320	64.8521	1.853
Water	128	7,680	64.1392	0.733
Water	192	17,280	63.6726	0.000
Combined	64	1,920	14.2051	1.528
Combined	96	4,320	14.1107	0.853
Combined	128	7,680	14.0264	0.251
Combined	192	17,280	13.9913	0.000

Note: $\Delta t = 0.025$ s and $\delta = 0.10$ K. Differences are relative to the 192-cell-height result for each material.

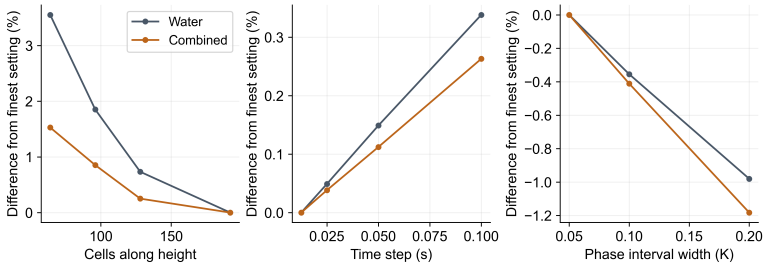


Figure 3. Numerical sensitivity of the 99% freezing time

Across the 12 nominal material cases, the largest final relative energy-balance residual was 7.34×10^{-13}. The boundary heat extraction and internal enthalpy change therefore agree to the stated numerical precision. Together, the analytical comparison, resolution tests, and heat-balance check give separate evidence for front tracking, discretization sensitivity, and conservation.

4 Results

4.1 Separate and Combined Material Effects

Table 5 compares the four endpoint materials under identical geometry and thermal conditions. Water reached a mean solid fraction of 0.99 after 64.92 s. At $\phi = 0.045$, particles alone reduced this time to 55.95 s, a reduction of 13.81%. Copper foam at $\gamma = 0.95$ reduced the pure-water-medium time to 15.14 s. The combined material reached the same endpoint in 14.12 s, giving an overall reduction of 78.25% relative to water.

Table 5. Charging performance and latent capacity under nominal conditions

Material	t_{99} (s)	q_{lat} ($\mathrm{MJ \cdot m^{-3}}$)	l ($\mathrm{kJ \cdot kg^{-1}}$)	P_{99} ($\mathrm{MW \cdot m^{-3}}$)
Water	64.92	333.60	333.60	5.087
Particles	55.95	318.59	257.80	5.637
Foam	15.14	316.92	226.70	20.717
Particles + foam	14.12	302.66	186.59	21.219

Note: Capacities are based on storage-region volume and composite mass, excluding fins and external containment.

The foam-only control separates the two material mechanisms. Adding foam to the particle-containing medium reduced its t_{99} by 74.76%, whereas adding particles to the foam-containing medium reduced t_{99} by 6.76%. The latter increment is smaller because the conductive skeleton already carries a substantial share of the heat transfer. The comparison attributes the main time reduction to the connected metallic network with a smaller additional contribution from particle loading.

4.2 Phase-Front and Temperature Development

Figures 4 and 5 present the solid fraction and temperature at the same three times for all four endpoint materials. At 5 s, freezing has progressed from the cooled wall and the two fin surfaces, leaving liquid toward the wavy boundary

and within thermally remote parts of the cell. The foam-containing materials show a more advanced front at this early stage. The two fields are linked by the same phase relation, so the residual liquid corresponds to temperatures close to the phase-change interval.

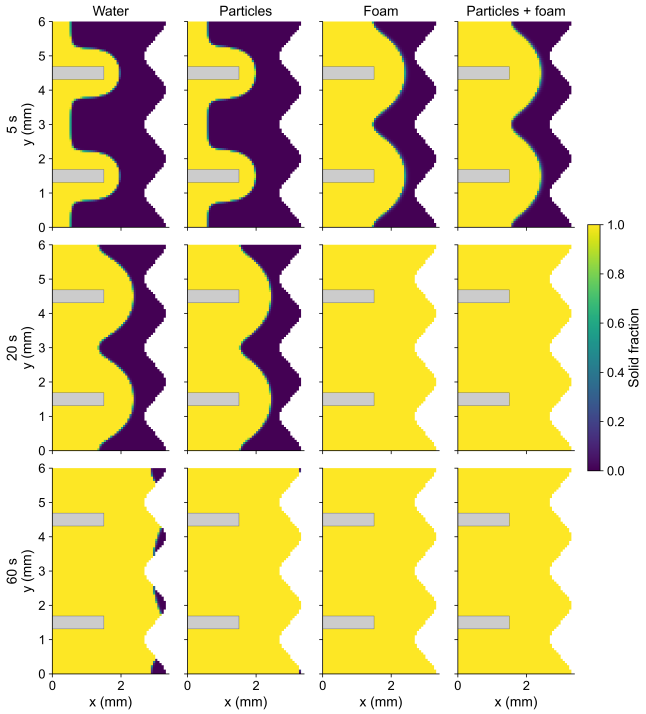


Figure 4. Solid-fraction distributions for the four endpoint materials

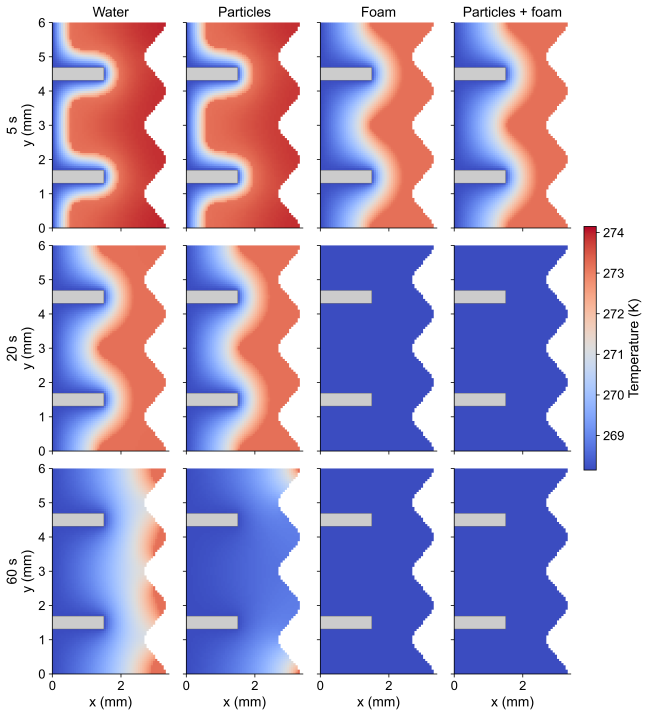


Figure 5. Temperature distributions for the four endpoint materials

By 20 s, both foam-containing cases have passed the 99% endpoint, while the foam-free media retain a larger liquid region. At 60 s, the particle-only medium has passed its endpoint and water is close to completing the transition. Temperature continues to fall after the latent transition as the solid composite approaches the cooled-boundary temperature. Comparing the fields at common times therefore reveals both the phase-change advance and

the subsequent sensible cooling.

The transient responses in Figure 6 show that the copper network accelerates both phase conversion and subsequent sensible cooling. Once solidification is complete, the mean temperature continues toward the cooled-wall temperature while the latent inventory reaches a composition-dependent plateau. Water retains the largest final latent inventory because it occupies the full storage-region volume.

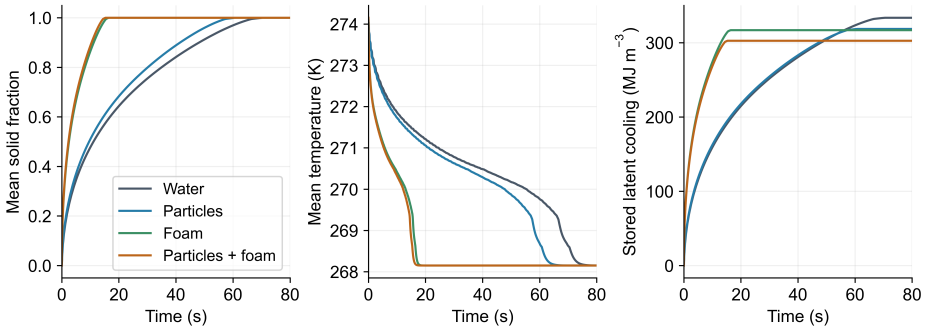


Figure 6. Evolution of mean solid fraction, mean temperature, and stored latent cooling for the four endpoint materials

4.3 Parameter Matrix and Material Capacity

Across the 12 material combinations in Figure 7, particle loading and porosity exert distinct effects on charging. Increasing particle loading shortens t_{99} at each porosity, and reducing porosity produces the larger shift. The effect of particle loading is strongest in the foam-free medium and becomes less pronounced as the skeleton contribution increases. At $\gamma = 0.95$, the copper network dominates the time reduction over the full particle-loading range.

The full latent capacity follows the water volume fraction $\gamma(1-\phi)$. The combined endpoint retains 90.73% of the water-baseline capacity, equivalent to 302.66 MJ·m^{-3}. At the same time, P_{99} increases from 5.087 to 21.219 MW·m^{-3}. The resulting index ratio is 4.17. These values describe a faster transition with a smaller latent inventory in the same storage-region volume.

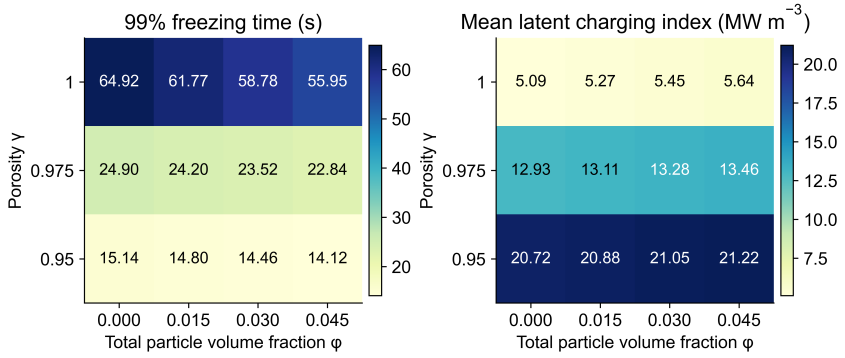


Figure 7. Effects of particle volume fraction and porosity on the 99% freezing time and average latent charging index

Composite mass introduces a stronger separation. Water has a mass-specific latent capacity of 333.6 kJ·kg^{-1} on the reference basis. The particle-only, foam-only, and combined materials give 257.8, 226.7, and 186.6 kJ·kg^{-1}, respectively. Dense silver particles and the copper skeleton add mass while displacing water. Figure 8 places this mass penalty alongside the volume-based charging-time tradeoff. Material selection for a mass-constrained installation consequently differs from selection based only on t_{99}.

4.4 Finite Charging Windows and Skeleton Conductance

Figure 9 evaluates the latent cooling present at charging deadlines of 10, 20, 40, and 80 s. After 10 s, water and the particle-only medium had established 159.14 and 162.39 MJ·m^{-3}, while foam and the combined medium had established 273.92 and 268.29 MJ·m^{-3}. Thus, the foam-only configuration held more latent cooling at this deadline even though the combined material had the shorter t_{99}. A completion-time ranking and a deadline-based inventory ranking answer different design questions.

At 80 s, the corresponding inventories were 333.60, 318.59, 316.92, and 302.66 MJ·m^{-3}. As charging progresses toward completion, the water fraction increasingly determines the available latent inventory. The comparison therefore favors conductive additions most strongly when the charging period is restrictive, while longer periods give greater weight to retained storage material.

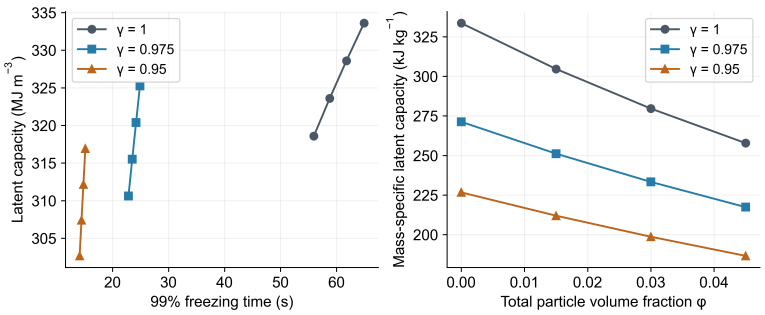


Figure 8. Charging-time and latent-capacity tradeoffs

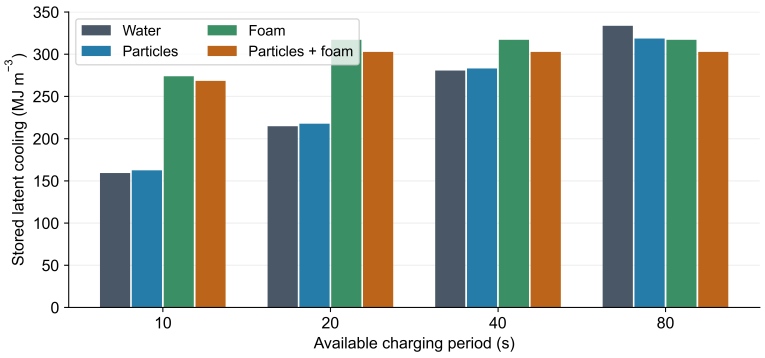


Figure 9. Stored latent cooling after charging periods of 10, 20, 40, and 80 s

The skeleton-factor calculation in Figure 10 holds $\phi = 0.045$ and $\gamma = 0.95$ while changing η. The combined-medium t_{99} varies from 29.56 s at $\eta = 0.10$ to 5.67 s at $\eta = 1.00$, with 14.12 s at the nominal factor 1/3. All three skeleton assumptions retain the same water volume. Their different charging times therefore isolate the conductive-network representation. The foam-only comparison follows the same evaluation, showing how particle addition interacts with the assumed skeleton effectiveness.

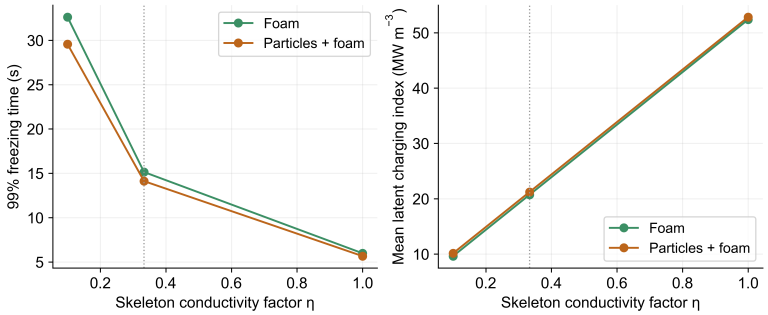


Figure 10. Effect of skeleton conductance on charging performance

5 Discussion

5.1 Conductive Allocation and the Choice of Design Objective

The foam-only control isolates the incremental effect of particles after the main conductive network has been established. At fixed porosity, particle addition changes both the pore-medium conductivity and the latent inventory, so its value depends on the charging deadline and the required cooling capacity. Studies of fin–foam and partially filled structures likewise treat the location and quantity of metal as design variables [12, 16, 17, 19]. The present matrix

extends that material-allocation question by reporting the same endpoint, capacity basis, and charging deadlines for each composition.

At $\gamma = 0.95$, adding $\phi = 0.045$ particles increases P_{99} by 2.42% relative to foam alone, while the mass-specific latent capacity falls from 226.7 to 186.6 kJ·kg^{-1}. The additional particle loading is therefore a comparatively small rate adjustment in a medium whose main conductive path is already metallic. This supports assessing particle use against an explicit charging requirement and material inventory, and selecting a loading that matches those requirements. Suspension stability and repeatable phase-change behavior remain relevant material-selection considerations established in experimental storage studies [21–24].

For equal full latent capacity on a storage-material basis, the combined medium requires 10.22% more volume and 78.78% more composite mass than water. These inventory ratios follow from the capacity values in Table 5 and exclude the cooled fins and external containment. They quantify the material commitment associated with the nominal charging-rate gain.

The finite-window result also clarifies the role of the charging index. P_{99} averages the latent inventory established up to a material-specific completion time. A fixed deadline instead compares inventories after the same operating duration. Both are useful, but their reference periods differ. The higher P_{99} of the combined material and the larger 10 s inventory of the foam-only medium are compatible outcomes of those definitions. Selecting an objective that matches the cooling duty is consequently as important as selecting a conductive composite.

5.2 Relevance to Sustainable Cooling Operation

Sustainable cooling requires coordination between cold production, electricity availability, and the cooling load. Control studies place this coordination at system level [1–3]. The present benchmark supplies component-level quantities for that task: a defined freezing endpoint, a latent inventory as a function of the charging deadline, and material capacity on volume and mass bases. A restricted production period can favor a conductive skeleton, whereas a longer period increases the value of retaining water. These quantities can be passed to a cooling-system calculation with its refrigeration coefficient of performance, storage heat losses, discharge schedule, and electricity profile.

The distinction between charging rate and refrigeration electricity is important for interpreting the engineering contribution. The reference cell imposes a cooled-boundary temperature and resolves the resulting heat transfer. Its sustainability assessment concerns the allocation of phase-changing material and the timing of cold production. System operation determines how that thermal response translates into electricity demand and resource use over repeated cycles. Full-cycle studies of composite stores provide a complementary basis for extending the component comparison to charging and discharge together [16, 20].

5.3 Model Scope and Extension to Storage Hardware

The calculations define an idealized local-thermal-equilibrium conduction benchmark with cooled fins and temperature-independent constituent inputs. This representation provides a common basis for material comparisons. The skeleton factor explicitly exposes the influence of the assumed network conductance, and the resolution checks quantify the numerical sensitivity of the reference cell. A hardware-specific application can assign effective conductivities from measured foam morphology and contact conditions, introduce the actual heat-transfer-fluid boundary, and examine the resulting full operating cycle. Experimental fin–foam and ice-storage investigations supply relevant configurations for that progression [17, 18].

6 Conclusions

This study examined the tradeoff between charging performance and material requirements in a wavy-walled cold thermal energy storage cell containing cooled fins, TiO_2–Ag–Al_2O_3 particles, and a copper conductive network. A conservative enthalpy model, verified against a two-phase Stefan solution and assessed through numerical refinement, separated the contributions of particles and foam across 12 material configurations. The comparison established how freezing time, retained latent capacity, and composite mass jointly influence material selection.

The copper network accounted for the dominant reduction in freezing time. Under the nominal conditions, the time to reach a mean solid fraction of 0.99 decreased from 64.92 s for water to 55.95 s with particles, 15.14 s with foam, and 14.12 s with both. The combined configuration reduced freezing time by 78.25% relative to water, whereas adding particles to the foam provided a further reduction of 6.76%. These findings identify network conductance as the primary design variable, with particle loading providing a smaller adjustment once the metallic pathway is established.

Faster phase conversion was accompanied by lower latent capacity and greater material requirements. The combined medium retained 90.73% of the water-baseline volumetric latent capacity and achieved an average latent charging index 4.17 times the baseline value. Its mass-specific latent capacity, however, decreased to 186.6 kJ·kg^{-1}. At equal full latent capacity, this composition required 10.22% more storage-material volume and 78.78% more composite mass than water. Charging deadlines also changed the preferred configuration: after 10 s, foam alone

stored 273.92 MJ·m^{-3}, exceeding the combined medium's 268.29 MJ·m^{-3} despite its longer freezing time. Material selection therefore depends on the cooling inventory required within the available charging period.

For sustainable cooling, these results support allocating conductive material according to both charging constraints and retained storage capacity. A copper network is particularly effective when rapid charging is required, while additional particles should be assessed against their incremental charging gain and associated capacity and mass penalties. The resulting performance measures provide component-level inputs for storage sizing and cooling-production scheduling. Further research should connect morphology-dependent network conductivity with complete charging–discharging cycles and refrigeration-system operation to assess electricity use and material requirements over repeated service.

Data Availability

The data used to support the research findings are available from the corresponding author upon request.

Conflicts of Interest

The author declares no conflicts of interest.

References

[1] H. Wang, B. Xie, and C. Li, "Review on operation control of cold thermal energy storage in cooling systems," *Energy Built Environ.*, vol. 6, pp. 509–523, 2025. https://doi.org/10.1016/j.enbenv.2024.01.007

[2] Z. Ouaouja, A. Ousegui, C. Toublanc, O. Rouaud, and M. Havet, "Phase change materials for cold thermal energy storage applications: A critical review of conventional materials and the potential of bio-based alternatives," *J. Energy Storage*, vol. 110, p. 115339, 2025. https://doi.org/10.1016/j.est.2025.115339

[3] F. L. Rashid, M. A. Al-Obaidi, A. Dulaimi, L. F. A. Bernardo, Z. A. A. Redha, H. A. Hoshi, H. B. Mahood, and A. Hashim, "Recent advances on the applications of phase change materials in cold thermal energy storage: A critical review," *J. Compos. Sci.*, vol. 7, p. 338, 2023. https://doi.org/10.3390/jcs7080338

[4] Y. Ma, Y. Tao, D. L. Deng, Y. Wang, and J. Y. Tu, "Experimental and numerical investigation on the charging and discharging process of a cold energy storage for space cooling of buildings," *Renew. Energy*, vol. 222, p. 119974, 2024. https://doi.org/10.1016/j.renene.2024.119974

[5] T. Reboli, M. Ferrando, A. Traverso, and J. N. W. Chiu, "Thermal energy storage based on cold phase change materials: Discharge phase assessment," *J. Energy Storage*, vol. 73, p. 108939, 2023. https://doi.org/10.1016/j.est.2023.108939

[6] Q. Ying, H. Wang, and E. Lichtfouse, "Numerical simulation on thermal behavior of partially filled metal foam composite phase change materials," *Appl. Therm. Eng.*, vol. 229, p. 120573, 2023. https://doi.org/10.1016/j.applthermaleng.2023.120573

[7] Z. L. Yang, R. Walvekar, W. P. Wong, R. K. Sharma, S. Dharaskar, and M. Khalid, "Advances in phase change materials, heat transfer enhancement techniques, and their applications in thermal energy storage: A comprehensive review," *J. Energy Storage*, vol. 87, p. 111329, 2024. https://doi.org/10.1016/j.est.2024.111329

[8] H. Li, Z. Liu, C. Nie, Q. Duan, C. Hu, D. Tang, and Z. Rao, "Thermal effect of the anisotropic metal foam on the melting performance of phase change material: A pore-scale study," *Int. Commun. Heat Mass Transfer*, vol. 159, p. 107995, 2024. https://doi.org/10.1016/j.icheatmasstransfer.2024.107995

[9] B. Buonomo, M. R. Golia, O. Manca, and S. Nardini, "A review on thermal energy storage with phase change materials enhanced by metal foams," *Therm. Sci. Eng. Prog.*, vol. 53, p. 102732, 2024. https://doi.org/10.1016/j.tsep.2024.102732

[10] I. Kaur, R. L. Mahajan, and P. Singh, "Generalized correlation for effective thermal conductivity of high porosity architectured materials and metal foams," *Int. J. Heat Mass Transfer*, vol. 200, p. 123512, 2023. https://doi.org/10.1016/j.ijheatmasstransfer.2022.123512

[11] C. Naldi, M. Dongellini, and G. L. Morini, "The evaluation of the effective thermal conductivity of metal-foam loaded phase change materials," *J. Energy Storage*, vol. 51, p. 104450, 2022. https://doi.org/10.1016/j.est.2022.104450

[12] C. Chen, Y. Diao, Y. Zhao, T. Zhu, Z. Wang, Y. Han, and Y. Liu, "Performance prediction of a fin–metal foam–cold thermal energy storage device: Solidification," *Int. J. Heat Mass Transfer*, vol. 202, p. 123672, 2023. https://doi.org/10.1016/j.ijheatmasstransfer.2022.123672

[13] Z. Du, G. Liu, X. Huang, T. Xiao, X. Yang, and Y. L. He, "Numerical studies on a fin-foam composite structure towards improving melting phase change," *Int. J. Heat Mass Transfer*, vol. 208, p. 124076, 2023. https://doi.org/10.1016/j.ijheatmasstransfer.2023.124076

[14] J. Zhang, Z. Cao, S. Huang, X. Huang, Y. Han, C. Wen, J. H. Walther, and Y. Yang, "Solidification performance improvement of phase change materials for latent heat thermal energy storage using novel branch-structured fins and nanoparticles," *Appl. Energy*, vol. 342, p. 121158, 2023. https://doi.org/10.1016/j.apenergy.2023.121158

[15] M. T. Alam, A. Raj, L. K. Singh, and A. K. Gupta, "Configurational assessment of solidification performance in a triplex-tube heat exchanger filled with composite phase change material," *Appl. Therm. Eng.*, vol. 230, p. 120814, 2023. https://doi.org/10.1016/j.applthermaleng.2023.120814

[16] Z. Du, X. Huang, Y. Li, X. Yang, and M. J. Li, "Design and study of metal foam parameters on whole melting-solidification cycle in phase change heat storage system," *Int. J. Heat Fluid Flow*, vol. 106, p. 109299, 2024. https://doi.org/10.1016/j.ijheatfluidflow.2024.109299

[17] X. Huang, Z. Du, Y. Li, Z. Li, X. Yang, and M. J. Li, "Optimal design on fin-metal foam hybrid structure for melting and solidification phase change storage: An experimental and numerical study," *Energy*, vol. 302, p. 131813, 2024. https://doi.org/10.1016/j.energy.2024.131813

[18] M. Xing, Z. Zhang, D. Jing, and H. Chen, "Enhanced solidification/melting heat transfer process by multiple copper metal foam for ice thermal energy storage," *J. Energy Storage*, vol. 79, p. 110207, 2024. https://doi.org/10.1016/j.est.2023.110207

[19] W. Chen, H. Wang, Q. Ying, and Y. Diao, "Heat transfer study of metal foam with partial filling method to strengthen phase change material," *Int. J. Refrig.*, vol. 165, pp. 245–256, 2024. https://doi.org/10.1016/j.ijrefrig.2024.05.002

[20] X. Huang, Z. Du, J. Guo, Y. Xie, X. Yang, and B. Sundén, "Numerical study on melting-solidification cycle of phase change energy storage unit: Role of fin and metal foam hybrid structure," *Int. Commun. Heat Mass Transfer*, vol. 163, p. 108776, 2025. https://doi.org/10.1016/j.icheatmasstransfer.2025.108776

[21] P. Sundaram, A. Kalaisselvane, A. Sathishkumar, P. GaneshKumar, S. C. Kim, and R. Prabakaran, "Synthesis, stability, and heat transfer behavior of water and graphene nanoplatelet-based nanofluid for cool thermal storage applications," *J. Energy Storage*, vol. 64, p. 107219, 2023. https://doi.org/10.1016/j.est.2023.107219

[22] N. K. Srinivasan and C. Ponnusamy, "Stability, thermal and solidification behaviour of oxygen functionalized GNPs–CuO/water-based hybrid nanofluid phase change materials for cool thermal energy storage system," *J. Energy Storage*, vol. 98, p. 113107, 2024. https://doi.org/10.1016/j.est.2024.113107

[23] S. I. Ibrahim, A. H. Ali, S. A. Hafidh, M. T. Chaichan, H. A. Kazem, J. M. Ali, W. N. R. Isahak, and A. Alamiery, "Stability and thermal conductivity of different nano-composite material prepared for thermal energy storage applications," *S. Afr. J. Chem. Eng.*, vol. 39, pp. 72–89, 2022. https://doi.org/10.1016/j.sajce.2021.11.010

[24] B. Prabhu and A. Valan Arasu, "Stability analysis of TiO_2–Ag nanocomposite particles dispersed paraffin wax as energy storage material for solar thermal systems," *Renew. Energy*, vol. 152, pp. 358–367, 2020. https://doi.org/10.1016/j.renene.2020.01.043

[25] W. Al-Kouz, W. Owhaib, A. Ayub, B. Souayeh, M. Hader, R. Z. Homod, T. Muhammad, A. Ishak, and U. Khan, "Thermal proficiency of magnetized and radiative cross-ternary hybrid nanofluid flow induced by a vertical cylinder," *Open Phys.*, vol. 22, no. 1, p. 20230197, 2024. https://doi.org/10.1515/phys-2023-0197

[26] M. Mirparizi, "Thermophysical enhancement of cold energy storage systems using metal foam and ternary nanoparticles: A numerical investigation," *Power Eng. Eng. Thermophys.*, vol. 5, no. 1, pp. 83–92, 2026. https://doi.org/10.56578/peet050105

[27] A. Shafee, "Coupled heat transfer and phase change in a porous nanofluid-enhanced cold thermal energy storage system: An adaptive mesh-based numerical study," *J. Complex Multiphys. Eng. Syst.*, vol. 1, pp. 98–109, 2026. https://doi.org/10.56578/jcmes010106

[28] J. N. Abu-Hamdeh and X. Zeng, "Solidification in a finned cold thermal energy storage unit for sustainable cooling: Effects of metal foam, hybrid nanoparticles, and radiative transfer," *J. Sustain. Energy*, vol. 5, no. 3, pp. 181–194, 2026. https://doi.org/10.56578/jse050301

[29] Y. A. Rothan, "Heat transfer treatment of system during freezing with implement of nanoparticles," *Case Stud. Therm. Eng.*, vol. 58, p. 104410, 2024. https://doi.org/10.1016/j.csite.2024.104410

[30] M. Rokhforouz, M. R. Dadashzadeh, and M. J. Sarmadi, "Numerical assessment of thermal energy storage in a triplex-tube heat exchanger with Al_2O_3-enhanced phase change material and tree-shaped fins," *J. Complex Multiphys. Eng. Syst.*, vol. 1, pp. 415–427, 2026. https://doi.org/10.56578/jcmes010407

[31] S. Savvopoulos, K. El Kadi, H. Zhang, and I. Janajreh, "Droplet freeze desalination high fidelity modeling for sustainable water purification and diverse applications," *Desalination*, vol. 586, p. 117858, 2024. https://doi.org/10.1016/j.desal.2024.117858

[32] M. L. Huber, R. A. Perkins, D. G. Friend, J. V. Sengers, M. J. Assael, I. N. Metaxa, K. Miyagawa, R. Hellmann, and E. Vogel, "New international formulation for the thermal conductivity of H_2O," *J. Phys. Chem. Ref. Data*, vol. 41, p. 033102, 2012. https://doi.org/10.1063/1.4738955

[33] R. Feistel and W. Wagner, "A new equation of state for H_2O ice Ih," *J. Phys. Chem. Ref. Data*, vol. 35, no. 2,

pp. 1021–1047, 2006. https://doi.org/10.1063/1.2183324

[34] A. Kondo, H. Matsuura, and Y. Ito, "Numerical study on effect of contact and interfacial resistance on thermal conductivity of dispersed composites," *Materials*, vol. 16, no. 2, p. 517, 2023. https://doi.org/10.3390/ma16020517

[35] B. J. Kaaks, M. Rohde, J. L. Kloosterman, and D. Lathouwers, "An energy-conservative DG-FEM approach for solid–liquid phase change," *Numer. Heat Transfer Part B Fundam.*, vol. 84, no. 5, pp. 487–513, 2023. https://doi.org/10.1080/10407790.2023.2211231

[36] B. J. Kaaks, M. Rohde, J. L. Kloosterman, and D. Lathouwers, "A finite volume parallel adaptive mesh refinement method for solid-liquid phase change," *Numer. Heat Transfer Part B Fundam.*, vol. 87, no. 1, p. 2387841, 2026. https://doi.org/10.1080/10407790.2024.2387841

[37] M. Colera, M. Freire-Torres, and J. Carpio, "Comparison of implicit enthalpy methods for Stefan problems," *Comput. Math. Appl.*, vol. 198, pp. 93–105, 2025. https://doi.org/10.1016/j.camwa.2025.08.015

[38] M. Sheikholeslami, "Efficacy of porous foam on discharging of phase change material with inclusion of hybrid nanomaterial," *J. Energy Storage*, vol. 62, p. 106925, 2023. https://doi.org/10.1016/j.est.2023.106925

[39] M. Sheikholeslami, "Numerical simulation for solidification in a LHTESS by means of nano-enhanced PCM," *J. Taiwan Inst. Chem. Eng.*, vol. 86, pp. 25–41, 2018. https://doi.org/10.1016/j.jtice.2018.03.013

[40] A. Boroojerdian, H. Nemati, and E. Selahi, "Direct and non-contact measurement of liquid fraction in unconstrained encapsulated PCM melting," *Energy*, vol. 284, p. 129359, 2023. https://doi.org/10.1016/j.energy.2023.129359